Vertical Motions in Orographic Cloud Systems over the Payette River Basin. Part 1: Recovery of Vertical Motions and their Uncertainty from Airborne Doppler Radial Velocity Measurements

Troy J. Zaremba[1], Robert M. Rauber[1], Samuel Haimov[1], Bart Geerts[2], Jeffrey R. French[2], Coltin Grasmick[2], Kaylee Heimes[1], Sarah A. Tessendorf[3], Katja Friedrich[4], Lulin Xue[3], Roy M. Rasmussen[3], Melvin L. Kunkel[5], and Derek R. Blestrud[5]

[1]Department of Atmospheric Sciences, University of Illinois Urbana-Champaign, Urbana, Illinois

[2]Department of Atmospheric Sciences, University of Wyoming, Laramie, Wyoming

[3]Research Applications Laboratory, National Center for Atmospheric Research, Boulder, Colorado

[4]Department of Atmospheric and Oceanic Sciences, University of Colorado Boulder, Boulder, Colorado

[5]Department of Resource Planning and Operations, Idaho Power Company, Boise, Idaho

Revision submitted to the Journal of Applied Meteorology and Climatology

Corresponding Author:
Troy J. Zaremba
University of Illinois Urbana-Champaign
4044 Natural History Building
1301 W. Green St
Urbana, IL, 61801
815-245-0031
tzaremb2@illinois.edu

ABSTRACT

Vertical motions over the complex terrain of Idaho's Payette River Basin were observed by the Wyoming Cloud Radar (WCR) during 23 flights of the Wyoming King Air during the SNOWIE field campaign. The WCR measured radial velocity, V_r, which includes the reflectivity-weighted terminal velocity of hydrometeors (V_t), vertical air velocity (*w*), horizontal wind contributions as a result of aircraft attitude deviations, and aircraft motion. Aircraft motion was removed through standard processing. To retrieve vertical radial velocity (W), V_r was corrected using rawinsonde data and aircraft attitude measurements. *w* was then calculated by subtracting the mean W, $(\overline{W})$, at a given height along a flight leg long enough for $\overline{W}$ to equal the mean reflectivity weighted terminal velocity, $\overline{V_t}$, at that height.

The accuracy of the *w* and $\overline{V_t}$ retrievals were dependent on satisfying assumptions along a given flight leg that the winds at a given altitude above/below the aircraft did not vary, the vertical air motions at a given altitude sum to 0 m s^{-1}, and $\overline{V_t}$ at a given altitude did not vary. The uncertainty in the *w* retrieval associated with each assumption is evaluated. Case studies and a project wide summary show that this methodology can provide estimates of *w* that closely match gust probe measurements of *w* at the aircraft level. Flight legs with little variation in equivalent reflectivity factor at a given height and large horizontal echo extent were associated with the least retrieval uncertainty. The greatest uncertainty occurred in regions with isolated convective turrets or at altitudes where split cloud layers were present.

1. Introduction

Vertical air motion is a key variable in atmospheric dynamics and cloud microphysics studies. This variable is difficult to measure, and Doppler profiling radar estimates are further challenged by the "contamination" of vertical air motion by the fall velocity of the radar scatters (i.e., hydrometeors). Separately, there is much interest in the estimation of terminal velocity of hydrometeors, as it carries information about size and riming fraction.

A vertically-pointing Doppler radar can provide direct measurements of vertical particle motion through the depth of a cloud. For a truly vertically-pointing Doppler radar, the Doppler vertical radial velocity, W, is the sum of the reflectivity-weighted terminal velocity (V_t) and the vertical air velocity (w). Approaches to retrieve w from W with ground-based radars have focused on cold clouds and have employed different methodologies to estimate and remove V_t of ice from W (see review by Protat and Williams, 2011). One approach involves calculating the mean value of W, $\overline{W}$, at a given altitude, over a sufficient period of time or distance, with the assumption that the expected magnitude and number of updrafts and downdrafts are approximately equal so that the mean value of w, $\overline{w} = 0$, and the mean value of W, $\overline{W}$, is equal to the mean of V_t ($\overline{V_t}$). $\overline{V_t}$ can then be subtracted from individual values of W to retrieve estimates of w (Delanoë et al. 2007). A second approach, applicable to hydrometeors whose fall speed is strongly dependent on size (such as rain or hail), involves binning W measurements based on reflectivity. Provided that the number of data points within each reflectivity bin is sufficiently large such that the number and magnitude of updrafts and downdrafts within each bin are equal, $\overline{W} = \overline{V_t}$ in each reflectivity bin and $\overline{V_t}$ can be subtracted from W based on a unique value of $\overline{V_t}$ for each reflectivity value (e.g. Orr and Kropfli 1999; Protat et al. 2003; Delanoë et al. 2007). A third approach, applicable in ice clouds, estimates $\overline{V_t}$ based on a relationship between particle fall speeds and maximum dimensions of ice particles integrated over an observed or assumed ice particle size distribution (e.g., Mitchell 1996; Heymsfield and Iaquinta 2000), after which $\overline{V_t}$ is subtracted from individual measurements of W to obtain w (Babb et al. 1999; Deng and Mace 2006). A fourth approach, applicable to liquid clouds, uses Doppler spectrum and a Mie notch technique in order to retrieve w (Kollias et al. 2002). A fifth approach, used in airborne studies, applicable to unrimed snow, is to simply assume a constant value for V_t (e.g., Grasmick and Geerts 2020), since the reflectivity-weighted terminal velocity of unrimed ice particles is often between 0.5-1.2 m s^{-1} over much of the cloud depth in ice cloud environments (e.g., Rosenow et al. 2014). In airborne radar studies, this constant value $\overline{V_t}$

can be estimated as the difference between the flight-leg-mean values of W (obtained from radar above and below flight level) and w (obtained from a gust probe) (Grasmick and Geerts 2020).

The problem of using these methods to retrieve w from an airborne platform is more complicated because of the motion of the aircraft on which the radar is mounted. When a nominally vertically-pointing beam is actually oriented in a direction other than nadir or zenith and is not orthogonal to the aircraft velocity vector, the horizontal winds and the aircraft motion will contribute to the measured radial velocity (V_r).

Correcting V_r for platform motion requires the radar antenna beam-pointing vector and a coordinate transformation between the aircraft body fixed-reference frame and the ground-fixed reference frame that considers the three-dimensional aircraft motion vector. The transformation involves consideration of the pitch, roll, and yaw angles, and aircraft ground speed (Haimov and Rodi 2013). However, after correction for aircraft motion, residual biases in V_r remain due to the contribution of horizontal winds to V_r when the beam is not pointing at nadir or zenith. For example, Fig. 1 shows V_r, corrected for platform motion contribution, during an eastbound and subsequent westbound flight leg over the Payette River Basin by the University of Wyoming King Air (UWKA) Wyoming Cloud Radar (WCR; Pazmany et al. 1994; Wang et al. 2012) during the Seeded and Natural Orographic Wintertime Clouds: the Idaho Experiment (SNOWIE; Tessendorf et al. 2019). V_r in these figures is not corrected for horizontal wind contributions. These flight legs (Fig. 1) illustrate an example of a deep stratiform cloud with weak echo near cloud top and possible cloud top entrainment occurring, weak boundary layer turbulence, and a melting level at ~2.8 km decreasing in altitude along the eastern end of both flight legs. The data show clear biases in V_r on consecutive legs (positive eastbound and negative westbound) that resulted from horizontal winds being projected into the beam.

Heymsfield (1989) was the first to develop a transformation matrix to retrieve W by removing contributions from the horizontal wind and aircraft motion components of V_r. He tested his retrieval using an idealized vertical profile of the horizontal wind field to estimate retrieval uncertainty. If the beam-pointing vector is known in ground relative coordinates, the contribution to single Doppler V_r by the horizontal wind, as measured by a rawinsonde, can be added or subtracted from individual range gates given the beam pointing direction (Geerts and Miao 2009). Both of these approaches assumed horizontal homogeneity of the horizontal winds. For airborne radars capable of providing multi-Doppler measurements, W can be retrieved via two- or three-dimensional Doppler velocity synthesis (Leon et al. 2006; Damiani and Haimov 2006; Hagen et al. 2021).

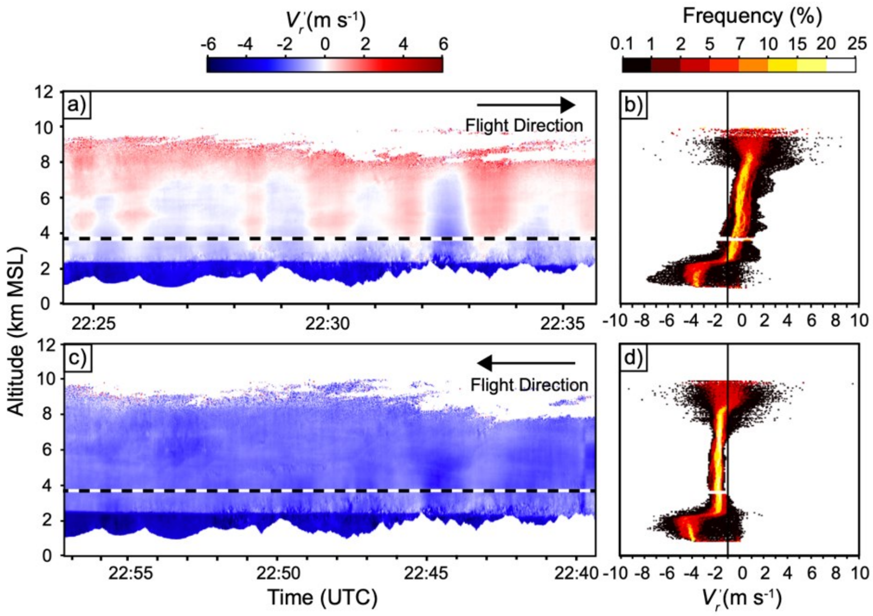

Fig. 1: V_r from IOP 23 during a consecutive east/west flight leg pair over the Payette River Basin. a) is the eastbound flight leg from 9 March 2017 22:24:00 to 22:35:42 UTC, and c) is the westbound flight leg from 9 March 2017 22:39:21 to 22:57:07 UTC. b and d are contoured frequency by altitude diagrams of V_r for the eastbound and westbound flight legs respectively, binned every 0.1 m s^{-1} every 100 m in altitude. The black vertical line on panels b and d denotes V_r of -1 m s^{-1}. In panels a and c, the dashed line is the altitude of the aircraft, and the white area below is the terrain.

Miao et al. (2006) commented on the horizontal wind contamination of the radial velocity from a non-vertically pointing airborne radar and the limited possibility of using a nearby sounding for correction, but did not use it. In order to remove the horizontal wind contribution using a rawinsonde, the assumption must be made that the flight legs occur over a short enough time and distance that the winds at a given altitude above/below the aircraft do not vary horizontally or change with time. Geerts and Miao (2009) applied this approach using rawinsonde winds with the WCR to retrieve W. However, their study did not include an uncertainty analysis regarding retrieved W and w. Geerts et al. (2011) and following studies (e.g. Bergmaier and Geerts 2016; 2017; 2020; Chu et al. 2017; Grasmick and Geerts 2020) have used horizontal wind profiles from rawinsondes in order to estimate the aircraft cross-track wind component and reduce error when performing dual-Doppler retrievals (Damiani and Haimov 2006). Bergmaier and Geerts (2017) noted that the use of other soundings (with different wind profiles) taken near the same time did not produce any significant differences in the recovered velocity field since aircraft attitude changes were small. French et al. (2015) used dual-Doppler synthesis (Damiani and Haimov, 2006) and instantaneous flight-level winds to retrieve the vertical plane two-dimensional velocity field. Pokharel et al. (2017) corrected nadir and zenith beams using a rawinsonde and noted that when the wind profile changes dramatically along a flight leg, there is higher uncertainty in w estimation especially when aircraft attitude changes were large. All of the studies quoted above use winds from a sounding profile to correct V_r "contaminated" by the horizontal wind to retrieve W but provide limited documentation and assessment of the effect of the rawinsonde correction algorithm on retrieval of w, its assumptions, and uncertainties.

An error in estimated W will also be present if there is an error in the antenna beam-pointing vector. The WCR beam-pointing vector, used herein, has been calibrated following Haimov and Rodi (2013). The maximum root mean square error in the calibrated beam-pointing angle is less than 0.1° resulting in less than 0.15 m s^{-1} error due to residual aircraft motion after removing the aircraft motion contribution.

To explore updraft retrievals under a variety of atmospheric conditions in complex terrain, we use herein aircraft observations from UWKA flown during SNOWIE. During the campaign, 23 research flights sampled orographic cloud systems over the Payette River Basin of Idaho. During flights the WCR made measurements of V_r within orographic cloud systems at high resolution (see Sec. 2a). During each research flight the UWKA flew along fixed tracks over the Payette River Basin parallel to mid-level (~700 hPa) flow (Fig. 2). One flight leg was typically completed in 10-20 minutes with 4-hour flights typically completing a total of 10-14 flight legs.

Flight legs sampled a variety of fixed (tied to the orography) and transient (related to vertical wind shear and conditional instability within passing weather systems) updrafts, providing a large dataset where w and $\overline{V_t}$ retrievals were possible using a rawinsonde wind correction after applying a series of assumptions regarding the horizontal wind and V_t. These assumptions include that i) the legs occur over a short enough time and distance that the horizontal winds at a given altitude above/below the aircraft did not vary horizontally or change with time, ii) the legs are also long enough that the magnitudes of the updrafts and downdrafts along a flight leg at any given altitude sum to 0 m s^{-1}, and iii) that the $\overline{V_t}$ did not vary substantially along the flight legs at a given altitude. The purpose of this study, Part 1, is to introduce and test the validity of these assumptions, and to evaluate the retrieval of w and $\overline{V}_t$ from the WCR using data from SNOWIE. In Part 2 (Zaremba et al. 2022), we quantify the magnitude, and associated uncertainties, of fixed and transient updraft structures over the Payette River Basin during SNOWIE and relate those updraft structures to the thermodynamic environments present during the project. In Part 3 (Heimes et al. 2022), we examine the impact of fixed and transient updrafts on trajectories of ice particles created by seeding clouds in both measured and simulated updraft fields over the Payette River Basin during SNOWIE cloud seeding operations.

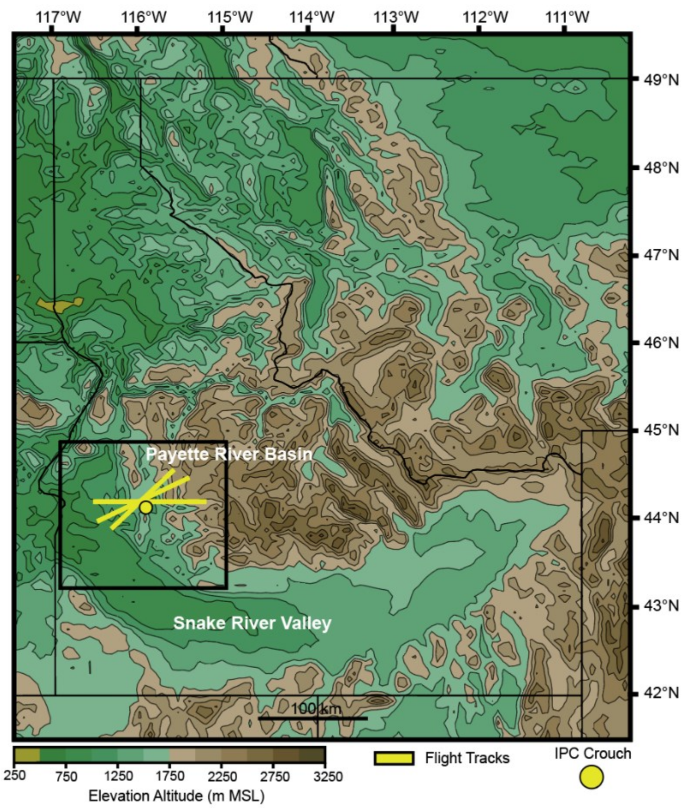

Fig. 2: Domain of SNOWIE (outlined in black) in Idaho. Terrain elevation in meters above mean sea level is contoured. Plotted in yellow are the three flight tracks flown during SNOWIE. Rawinsondes were launched by Idaho Power Company (IPC) at Crouch, Idaho denoted by a yellow circle.

This paper is organized as follows: Sec. 2 presents the data used in this analysis. Sec. 3 provides an overview of the retrieval methodology and assumptions required to retrieve w and $\overline{V}_t$. Sec. 4 evaluates retrieval uncertainty including a summary of uncertainty estimates using data from all research flights. Sec. 5 presents examples of retrieved w and $\overline{V}_t$ along flight legs. Sec. 6

examines conditions which can result in higher retrieval uncertainty and Sec. 7 quantifies retrieval uncertainties for all flight legs during SNOWIE. Key conclusions are discussed in Sec. 8.

2. Data

a) UWKA Wyoming Cloud Radar data

The WCR is a 95 GHz, 3 mm wavelength, pulsed Doppler cloud radar that was flown on the UWKA during SNOWIE. Data used herein are from the WCR fixed antennas nominally pointed at zenith and nadir during straight, level flight. In this configuration, the WCR measured the equivalent reflectivity factor (Z_e) and V_r. The WCR reflectivity is calibrated by measuring the return from a trihedral corner reflector with a known scattering cross-section. Error associated with this calibration is estimated to be less than 2.5 dB at any distance away from the radar flight level (Wendisch and Brenquier 2013, Ch. 9.5.5, pp. 509-517; Grasmick et al. 2022). The minimum detectable signal was ~-40 dBZ$_e$ at 1 km distance away from the radar and ~-26 dBZ$_e$ at a distance of 5 km. Data were sampled at 30 m in range along the radar beam and 4.5-7.5 m along the flight track depending on the speed of the UWKA. Only straight, level flight legs were used in this analysis.

The measured values of Z_e and V_r can be negatively impacted by attenuation, particularly in water clouds. Attenuation, under these conditions, can reduce the signal strength to the point of low signal to noise ratio. This would result in reduced Z_e and higher variance in V_r estimates. During SNOWIE, radar echoes were almost entirely due to ice. On a few flights, a very low-level melting level was present near the terrain. Protat et al. (2019) show that the two-way attenuation coefficient produced by stratiform ice particles at W-band ranges between 1 and 1.6 dB km^{-1} for W-band reflectivity values between 13 and 18 dBZ$_e$ with an increase in attenuation with reflectivity. At such high reflectivity values, W-band scattering largely falls in the Mie regime, i.e. reflectivity values for weather (cm-wave) radars are much higher. Figure 3a shows a Contoured Frequency by Altitude Diagram (CFAD) of WCR Z_e for the entire SNOWIE campaign (all 238 flight legs). Less than 1% of the measurements exceeded 19 dBZ$_e$ and less than 5% exceeded 12 dBZ$_e$. W-band power is also attenuated by cloud droplets: the two-way path-integrated attenuation rate is about 10 dB per km per g kg^{-1} of liquid water (Liebe et al. 1989; Vali and Haimov 2001). A microwave radiometer was located at Horseshoe, Idaho (just southwest of Crouch, Idaho; see Fig. 2). The radiometer provided measurements of vertical liquid water path every six minutes during SNOWIE on station flight times (Table 1). Data were not available for the March flights and were masked when liquid water was present on the radiometer dome. 90% of the values were below 1.03 mm (Fig. 3b). The aircraft flew at approximately 4 km altitude during SNOWIE, with about 2.5 km of cloud beneath the aircraft, and 1-6 km of cloud above the aircraft. The two-way attenuation rate for different cloud depths as a function of radiometric liquid water measurements appears in Fig. 3. If we assume that the cloud water was concentrated below the aircraft at warmer temperatures, the W-band two-way attenuation was less than 3.3 dB km^{-1} for 90% of the time the aircraft was flying. In this paper, horizontal variations in Z_e at a given level are used to quantitatively estimate uncertainties associated with retrieval of w and $\overline{V}_t$. Vertical variations in Z_e, where attenuation would be more prevalent, are not considered in this analysis. Since attenuation would lead to greater variation in Z_e at a given level, the effect of the attenuation would be to increase the calculated uncertainty in the retrieval of w.

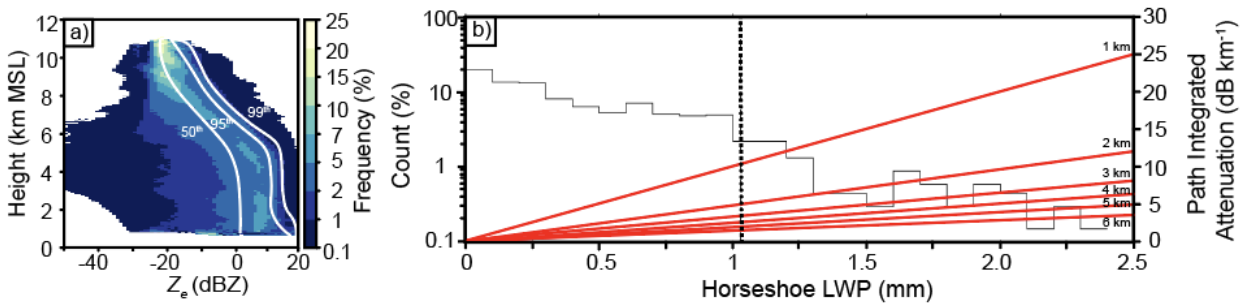

Fig. 3: a: CFAD of Z_e for all 238 SNOWIE research flight legs. The CFAD is binned every 100 m in altitude and every 1 dBZ$_e$. The frequency is normalized to 100% at each altitude bin. The 50th, 95th, and 99th quantiles are overlaid in white and labeled. b: (solid black line) distribution of vertically integrated liquid water path from a radiometer at Horseshoe, ID during SNOWIE aircraft on station sampling times in Table 1. Red lines represent the two-way path integrated attenuation for different cloud depths. The black dashed line represents the 90th percentile of the radiometer measurements.

b) Rawinsonde data

Special rawinsondes were launched over the Payette River Basin to analyze the thermodynamic properties and wind fields within the orographic cloud systems. The Idaho Power Company (IPC) launched Lockheed Martin LMS6 rawinsondes from Crouch, Idaho (Fig. 2) at regular intervals during research flights, typically every 2-3 hours. In this paper, we limit the use of the rawinsondes to measurement of the winds. The manufacturer-stated accuracy of IPC rawinsondes was ± 0.2 m s^{-1} for wind speed. Rawinsonde data collected during SNOWIE typically had an average vertical resolution of 4 m with the sondes recording data every second, ascending at ~5-6 m s^{-1}, and drifting an average of 12.4 km away from their launch location upon reaching cloud top.

c) UWKA gust probe data

During SNOWIE, horizontal winds and vertical velocity from a gust probe mounted on a nose boom on the UWKA were recorded at a rate of 1 Hz. Aircraft motion was removed from the gust probe raw winds to retrieve w_{gp} using aircraft speed and acceleration obtained from the Inertial Navigation System and aircraft attitude parameters. Because gust probe velocity components result from the integration of accelerations, their variations are known more accurately than their long-track mean. Therefore, it is customary to remove the long-track mean vertical velocity. After removal of leg averages, the resulting gust probe vertical velocity (w_{gp}) is accurate to at least 0.1 m s^{-1} (Lenschow 1972; Geerts and Miao 2005). This procedure was followed in this analysis. w_{gp} was linearly interpolated to match the sampling rate of the WCR.

3. Retrieval of vertical air motion and mean terminal fall velocity

The goal of this paper is to retrieve vertical profiles of vertical air motion, w, along flight legs, and a profile of reflectivity-weighted mean terminal velocity averaged along a flight leg, $\overline{V}_t$, from measurements of radial velocity, V_r, by an aircraft with radar beams nominally pointing at nadir or zenith, and estimate associated uncertainties. The retrieval technique first involves using rawinsonde-measured winds to retrieve W, the vertical hydrometeor velocity at a range gate, by removing contributions of the aircraft motion and the horizontal wind to V_r due to time-dependent variations in the beam-pointing vector. These result from small fluctuations in pitch, roll, and yaw of the aircraft due to flight-level turbulence or pilot adjustments while flying along straight flight legs.

The value of W at each range gate is retrieved using a horizontal wind profile derived from a rawinsonde, the ground-relative 3D aircraft motion vector, and the beam-pointing vector by performing a coordinate transform from the fixed aircraft reference frame to a ground reference frame. The transformation matrix (Haimov and Rodi, 2013) and method of retrieval of W from V_r are given in Appendix A.

Values of W were retrieved along each beam between the ground and cloud echo top except in a 250 m zone centered at flight level. W was then regridded to a common grid of 30 m vertical range referenced to mean sea level (all altitudes in this paper are with respect to mean sea level (MSL)). Range gates were resampled to the new grid using a nearest neighbor approach to estimate

$\overline{V}_t$ at a given height and preserve the original W values. There were m altitudes with valid measurements between the aircraft and ground (or cloud echo top), and n grid points along a given flight leg, so each flight leg had an $m \times n$ grid of retrieved W.

In order to retrieve w and $\overline{V}_t$ from W, three assumptions had to be made:

1. The horizontal wind, $\overrightarrow{V_H}$, is invariant at a given height, m, along a flight leg, and can be represented by the winds measured by a nearby rawinsonde.
2. The flight leg was sufficiently long such that at each m, $\overline{w_m} = \sum_1^n w_{m,n} = 0$ m s^{-1}. Simply stated, this assumption is that the sum of the magnitudes of the updrafts and downdrafts along the track at any altitude average to zero.
3. The reflectivity-weighted hydrometeor terminal velocity does not vary significantly along the leg at a given altitude, so that, at any point along the track, $V_{t,m} \cong \overline{V_{t,m}} = \sum_1^n V_{t,(m,n)}/n$.

Applying these assumptions:

$$\overline{V_{t,m}} = \overline{W_m}$$

and:

$$w_{(n,m)} = W_{(n,m)} - \overline{V_{t,m}}$$

In this manner, w can be retrieved for all $m \times n$ grid points on a flight leg and a $\overline{V}_t$ profile for that flight leg can be obtained. In the remainder of this paper, we test the validity of, and estimate the uncertainty associated with the three assumptions stated above and examine example retrievals of w and $\overline{V}_t$ in orographic clouds over the Payette River Basin.

4. Retrieval uncertainty

In this section, we evaluate the uncertainty in the estimates of w arising from violations of the assumptions stated in the previous section.

a) Assumption 1: The horizontal wind, $\overrightarrow{V_H}$, is invariant at a given height, m, along a flight leg, and can be represented by the winds measured by a nearby rawinsonde.

During SNOWIE flights, project rawinsondes were launched at Crouch, Idaho (see Sec. 2c), a site close to the flight track. The rawinsonde used to retrieve w for each flight can be found in Table 1. The average aircraft on-station sampling time was 2.5-3.5 hours with the rawinsonde typically launched during or near the sampling period. A difficulty with quantifying uncertainty associated with this assumption was that there were no measurements of the along-track variation of the horizontal wind above or below the aircraft flight level. The UWKA did however, measure the zonal, u, and meridional, v, components of the wind at flight level (m_{ac}) along each flight leg. These could be directly compared to sounding measurements. Flight level measurements will be used to provide a best available estimate of uncertainty due to differences in measured wind along a given flight leg between the aircraft and rawinsonde.

IOP	Rawinsonde Launch Time	On-Station Flight Time
1	8 January 2017 04 UTC	0246 UTC – 0540 UTC
2	9 January 2017 05 UTC	0435 UTC – 0727 UTC
3	11 January 2017 03 UTC	0247 UTC – 0528 UTC
4	18 January 2017 22 UTC	2017 UTC – 2351 UTC
5	19 January 2017 16 UTC	1541 UTC – 1822 UTC
6	20 January 2017 00 UTC	2245 UTC – 0152 UTC
7	21 January 2017 21 UTC	2249 UTC – 0128 UTC
8	22 January 2017 18 UTC	2118 UTC – 0020 UTC
9	31 January 2017 16 UTC	2021 UTC – 2201 UTC
10	3 February 2017 21 UTC	2006 UTC – 2125 UTC
11	4 February 2017 23 UTC	2209 UTC – 0107 UTC
12	7 February 2017 22 UTC	2013 UTC – 2303 UTC
13	16 February 2017 20 UTC	2343 UTC – 0041 UTC
14	18 February 2017 20 UTC	2139 UTC – 0041 UTC
15	19 February 2017 15 UTC	1744 UTC – 2046 UTC
16	20 February 2017 15 UTC	1447 UTC – 1721 UTC
17	21 February 2017 16 UTC	1443 UTC – 1807 UTC
19	4 March 2017 14 UTC	1330 UTC – 1642 UTC
20	5 March 2017 13 UTC	1213 UTC – 1444 UTC
21	7 March 2017 14 UTC	1423 UTC – 1736 UTC
22	9 March 2017 16 UTC	1422 UTC – 1646 UTC
23	9 March 2017 23 UTC	2019 UTC – 2332 UTC
24	16 March 2017 03 UTC	0108 UTC – 0420 UTC

Table 1: Rawinsonde launched at Crouch used to retrieve w during each SNOWIE Intensive Operation Period (IOP) research flight.

The only measure of the variability of the horizontal winds along the cross section were made by the aircraft at flight level. Flight level winds were compared to those measured by the rawinsonde at m_{ac}. The average difference and standard deviation between wind speed measured at flight level and wind speed measured by the rawinsonde for the entire SNOWIE field campaign was u = -0.7 ± 4.2 m s^{-1} and v = 0.0 ± 3.7 m s^{-1} (Fig. 4a,b). An uncertainty estimate (Δw) using

Appendix A Eq. 4 was calculated for each beam along a given flight leg using the difference in measured wind speeds between the sounding and gust probe to calculate the difference in w. In order to match rawinsonde winds with those measured at the aircraft flight level, sounding data were linearly interpolated to the nearest 0.1 m. Δw was calculated for both the nadir and zenith beams.

To estimate uncertainty along a given flight leg associated with assumption 1 the standard deviation of Δw ($\sigma_{w,1}$) for all nadir and zenith beams along a given leg was calculated. Figure 4c,d shows the distribution of Δw for all beams during the SNOWIE field campaign associated with violations of assumption 1. Δw had a standard deviation of 0.15 m s^{-1} for all zenith beams and 0.14 m s^{-1} for the nadir beams. $\sigma_{w,1}$ had a median of 0.06 m s^{-1} for all flight legs for both nadir and zenith beams (Fig. 4e,f). For most flight legs the uncertainty associated with $\sigma_{w,1}$ was less than 0.1 m s^{-1} (Fig. 4g). Intensive operation period (IOP) 13 may have had a greater uncertainty because the rawinsonde used to retrieve w was launched ~4 hours before the research flight, the largest difference for any IOP. In Sec. 5 we quantify $\sigma_{w,1}$ for specific flight legs during SNOWIE.

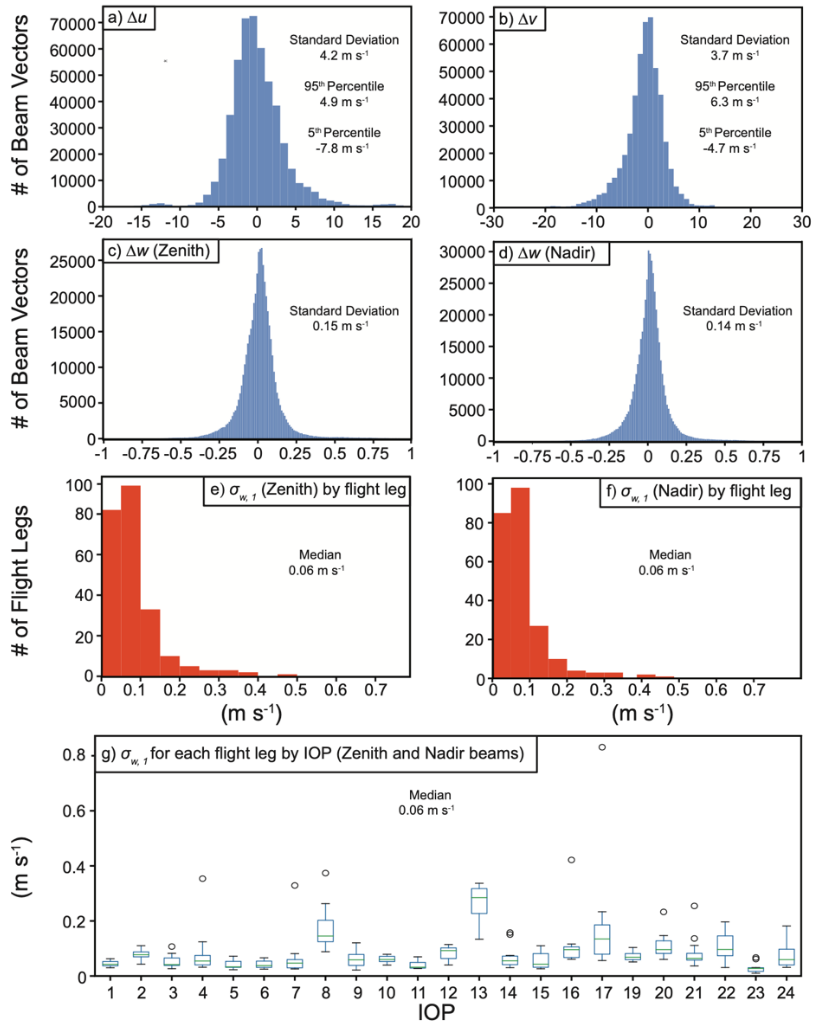

Fig. 4: (a) Δu: Difference in the u component of the wind speed measured by the aircraft at m_{ac} and the u component of the wind speed measured by the rawinsonde used to retrieve w. (b) Δv: Same as (a) except for the v component of the wind. (c) Δw for all zenith beams calculated using the difference in aircraft measured and sounding measured wind speed. (d) same as (c) except for the nadir beam. (e) $\sigma_{w,1}$ for zenith beams for all flight legs during SNOWIE. (f) Same as e except for nadir beams. (g) boxplot of $\sigma_{w,1}$ for nadir and zenith beams for all research flights during SNOWIE.

b) Assumption 2: $\overline{w_m} = \sum_1^n w_{m,n} = 0$ m s^{-1} along a flight leg

To estimate horizontal cloud extent needed at a given grid level m for $\overline{w_m} = 0$ m s^{-1}, the great circle distance between each grid column n on a given flight leg was calculated based on the latitude and longitude of the UWKA. Each flight leg was then broken up into units 2-120 km in length (in 2 km increments). For example, a flight leg 100 km in length was broken up into fifty 2 km units, twenty-five 4 km units, sixteen 6 km units, etc. Units could only be as long as the flight leg's maximum length. Only grid levels where radar echo was present across the entire flight leg were used in the uncertainty analysis. $\overline{w}$ was calculated at each m, along each unit. Figure 5 shows $\overline{w}$ for all segment lengths during SNOWIE normalized as a percentage of a given segment length (binned every 0.05 m s^{-1} and 2 km). The standard deviation of each segment length was then calculated and used to estimate the standard deviation of w associated with assumption 2 ($\sigma_{w,2}$) (see Fig. 5). The analysis shows that if horizontal echo extent was 2 km at a given m, $\sigma_{w,2}$ would be 0.46 m s^{-1}, while if the echo extent was 80 km at a given m, $\sigma_{w,2}$ would be 0.03 m s^{-1}. $\sigma_{w,2}$ approaches 0 m s^{-1} at leg lengths >80 km. The source of the increase in $\sigma_{w,2}$ beyond 80 km is uncertain, but may be related to the broader effect of ascent across the entire mountain massif of Idaho.

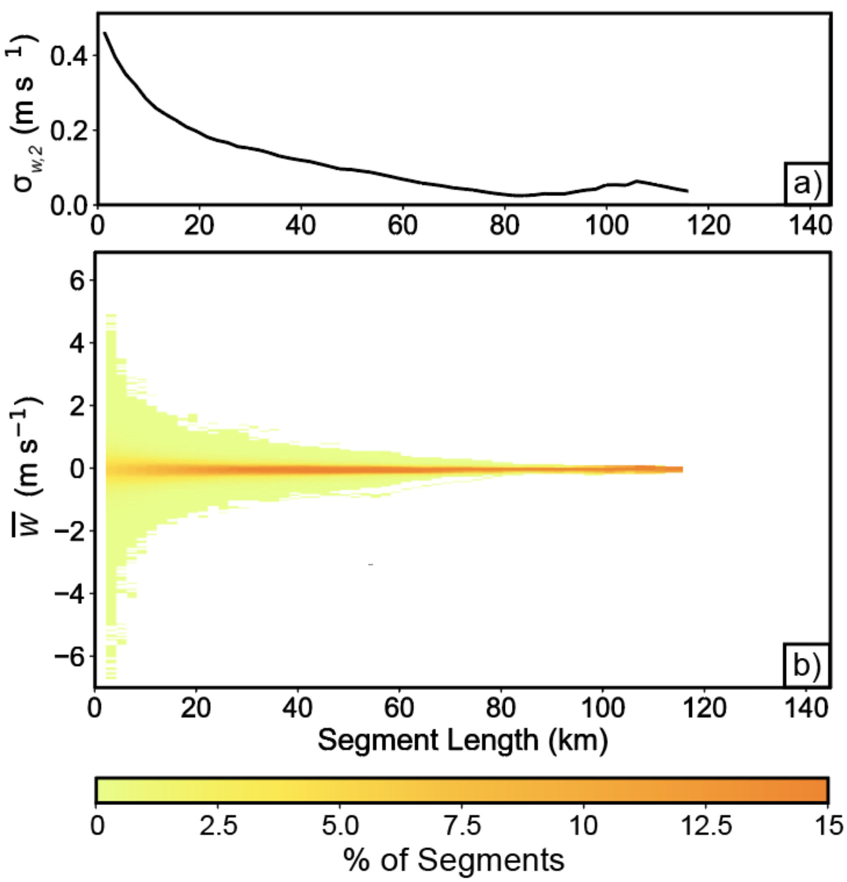

Fig. 5: $\overline{w}$ found using methodology presented in Sec. 4 for different segment lengths (2 km intervals). a: $\sigma_{w,2}$ for all segment lengths. b: distribution of $\overline{w}$ for each segment normalized as a percentage of all segments with a given segment length (binned every 0.05 m s^{-1} and 2 km).

c) Assumption 3: $V_{t,m} = \overline{V_{t,m}} = \sum_1^n V_{t,(m,n)}/n$ *along a flight leg*

Periods with large Z_e variation at a given level (m) would be expected to have large variation in $\overline{V_{t,m}}$. In order to estimate the standard deviation of w associated with assumption 3 ($\sigma_{w,3}$), the retrieved w at the first valid range gate above and below the UWKA were averaged and compared to vertical velocity measured by the gust probe at flight level (w_{gp}). w_{gp} was linearly interpolated to match the sampling rate of the WCR. The standard deviation of $|w - w_{gp}|$, ($\sigma_{|w-w_{gp}|}$), along a given flight leg was compared to the standard deviation of Z_e, (using logarithmic units), σ_{Z_e}, directly above and below the aircraft, also along a given flight leg, using the same range gates as radar-retrieved w (Fig. 6). $\sigma_{|w-w_{gp}|}$ was then estimated using a least squares line of best fit where

$$\sigma_{w,3} = \sigma_{|w-w_{gp}|} = 0.016 * \sigma_{Z_e} + 0.126.$$

At a given level m, σ_{Z_e} was calculated and the relationship above was used to estimate $\sigma_{w,3}$. For example, σ_{Z_e} of 15 dBZ$_e$ would have a $\sigma_{w,3}$ of 0.37 m s^{-1}, and a σ_{Z_e} of 1 dBZ$_e$ would have a $\sigma_{w,3}$ of 0.14 m s^{-1}.

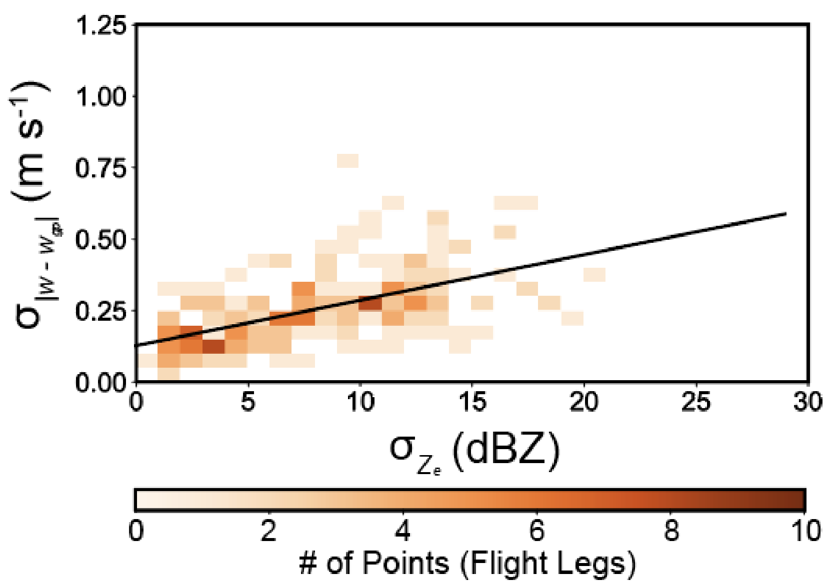

Fig. 6: A comparison of $\sigma_{|w-w_{gp}|}$ and σ_{Z_e} for all flight legs during SNOWIE. The black line represents the best fit line which is $\sigma_{w,3}$ or $\sigma_{|w-w_{gp}|} = 0.016 * \sigma_{Z_e} + 0.126$.

d) Total uncertainty of assumptions 1-3

The total retrieval uncertainty (σ_T) at a given m was estimated as:

$$\sigma_T = \sqrt{\sigma_{w,1}^2 + \sigma_{w,2}^2 + \sigma_{w,3}^2}$$

This assumes that the three errors are independent. Sec. 5 and 6 show examples of w retrieval and σ_T from specific flight legs during SNOWIE research flights. A summary of uncertainty for all SNOWIE research flights is presented in Sec. 7.

5. Retrieval examples and uncertainty estimates

a) IOP 23 9 March 2017

IOP 23 sampled a deep stratiform cloud within southwest flow over the Payette River Basin. Figure 7a shows an eastbound flight leg (22:24:40 to 22:35:35 UTC) over the terrain and reveals that V_r was ~1 m s^{-1} near cloud echo top. A Contour Frequency by Altitude diagram (CFAD) in Fig. 7b show V_r decreasing with depth beneath cloud echo top. Applying the retrieval methodology in Sec. 3, the retrieved w in Fig. 7c reveals weak orographic ascent extending through the cloud echo top on the windward (west) sides of mountains on the flight leg, and downslope flow on the leeward sides, with updrafts and downdrafts on the order of ± 0.5 m s^{-1} (Figs. 7d). Turbulence, and Z_e approaching the minimal detectable signal, is influencing V_r near cloud echo top. Turbulence in the boundary layer is also evident, with the CFAD in Fig. 7d showing w ranging from ± 3 m s^{-1} in both these regions. The w field in Fig. 7c suggests that it is meaningful to separate between *fixed updrafts*, i.e. part of the stationary wave pattern tied to the orography, and *transient updrafts*, i.e. more short-lived, advecting features associated with turbulence (in this case), or with small-scale convective instabilities within passing weather systems updrafts. This distinction is explored in detail in Part 2.

Note that at and below the melting level, errors in the retrieval are evident due to nonuniformity of the melting level. The cause of these errors will be addressed in the Sec. 6. The retrieved $\overline{V_t}$ was -0.2 m s^{-1} near cloud echo top, decreasing with depth beneath cloud echo top to ~ -1 m s^{-1}, and further decreasing to ~-4 m s^{-1} beneath the melting level.

Examining uncertainty associated with each of the three assumptions:

Assumption 1: $\sigma_{w,1}$ =± 0.03 m s^{-1} as a consequence of differences between wind speed measured at flight level and the rawinsonde (Fig. 7i).

Assumption 2: $\sigma_{w,2}$= ± 0.03 m s^{-1} between 2.3 and 7.9 km (Fig 7j) where echo extent encompassed the entirety of the 82.8 km flight leg. $\sigma_{w,2}$ = ± 0.47 m s^{-1} near the surface and within 200 m of cloud echo top, where echo extent was less than the length of the flight leg due to the terrain and cloud top variability. The implication is that assumption 2 loses validity (and w cannot be reliably retrieved) near the surface in the presence of complex terrain and near cloud top when the cloud top is uneven and Z_e approaches the minimum detectable signal, leading to increased variance in measured V_r.

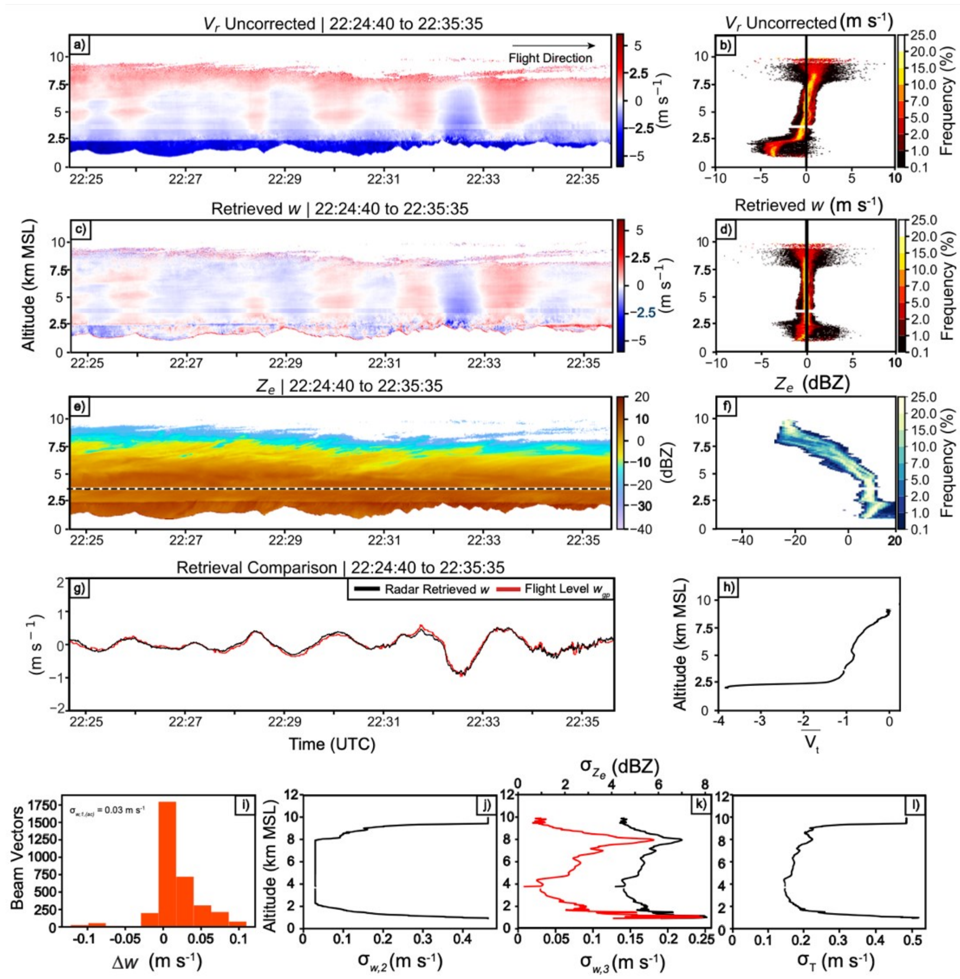

Fig. 7: Eastbound flight leg during IOP 23 from 9 March 2017 22:24:40 to 22:35:35 UTC. First row: (a) uncorrected V_r and (b) uncorrected V_r CFAD binned every 0.1 m s^{-1} and 100 m in altitude. Second row: (c) retrieved w and (d) accompanying CFAD binned every 0.1 m s^{-1} and 100 m in altitude. Third row: (e) Z_e cross section and (f) Z_e CFAD binned every 1 dBZ$_e$ and 100 m in altitude. Fourth row: (g) comparison of w_{gp} (red) at flight level with radar retrieved w (black) and (h) is the retrieved $\overline{V_t}$ profile. Fifth row: (i) ΔW for all nadir and zenith beams, (j) $\sigma_{w,2,m}$, (k) $\sigma_{Z_e,m}$(black) and $\sigma_{w,3,m}$ (red), and (l) $\sigma_{T,m}$. West is on the left and east on the right of the radar cross sections.

Assumption 3: $\sigma_{w,3} = \pm$ 0.13– 0.19 m s^{-1} between 1.5-7.6 km. In this layer, the Z_e CFAD (Fig. 7f) showed minimal variation in Z_e at all m with $\sigma_{Z_e} < 5$ dBZ$_e$ (Fig. 7k). This suggests that the ice particle ensemble observed were likely undergoing similar growth mechanisms at a given altitude. At 8 km and within 240 m near the surface, $\sigma_{w,3} = \pm 0.20$-0.25 m s^{-1}.

As a result, ± 0.14 m s^{-1} < σ_T < ± 0.21 m s^{-1} between 1.9 and 7.6 km increasing within 200 m of cloud echo top to ± 0.48 m s^{-1} and to ± 0.50 within 120 m of the surface (Fig. 7l).

To determine if σ_T was a reasonable estimate of uncertainty on a flight leg, w_{gp} was taken as truth and the mean absolute error (MAE) was calculated along a given flight leg as follows:

$$MAE = \frac{\sum_{i=1}^{k} \left| w_{gp} - w \right|}{k}$$

where k was the number of collocated gust probe/radar retrieval measurements along a given flight leg and the average radar retrieved w is from the first range gates above and below the aircraft averaged together. The comparison shows a close correspondence in time between the retrieved w and measured w_{gp} (Fig. 7g). MAE was 0.05 m s^{-1} along the flight leg, less than σ_T at the same altitude (±0.21 m s^{-1}).

b) IOP 21 7 March 2017

IOP 21 sampled a cloud system over the Payette River Basin that was on the north side of an extratropical cyclone. A V_r cross section from a northeast to southwest (16:13:00 to 16:27:50 UTC) flight leg revealed a split cloud layer (Fig. 8a). The lower cloud layer was predominantly stratiform with boundary layer turbulence present in the lowest kilometer near the terrain.

Retrieved w in Figs. 8c,d reveals broadscale orographic lift with updrafts on the windward, and downdrafts on the leeward sides of the mountains. Three regions of stronger updrafts ranging from -3 to 3 m s^{-1} are evident, the first near the terrain (< 2.5 km), the second near the top and base of the split in the cloud layers (between 5-6 km) and the third near cloud echo top (near 9 km) (Fig. 8d). At low levels, these are associated with terrain-induced turbulence and terrain-driven eddy dipoles (the wind is left to right). At higher levels, the main mechanism is mixing, likely due to evaporation and radiative cooling along cloud/clear boundaries, as well as Z_e approaching the minimum detectable signal. $\overline{V_t}$ was more variable in this case due to the split cloud layer, decreasing from near -0.1 m s^{-1} to ~ -1 m s^{-1} between cloud echo top and the base of the lower cloud layer (Fig. 8h).

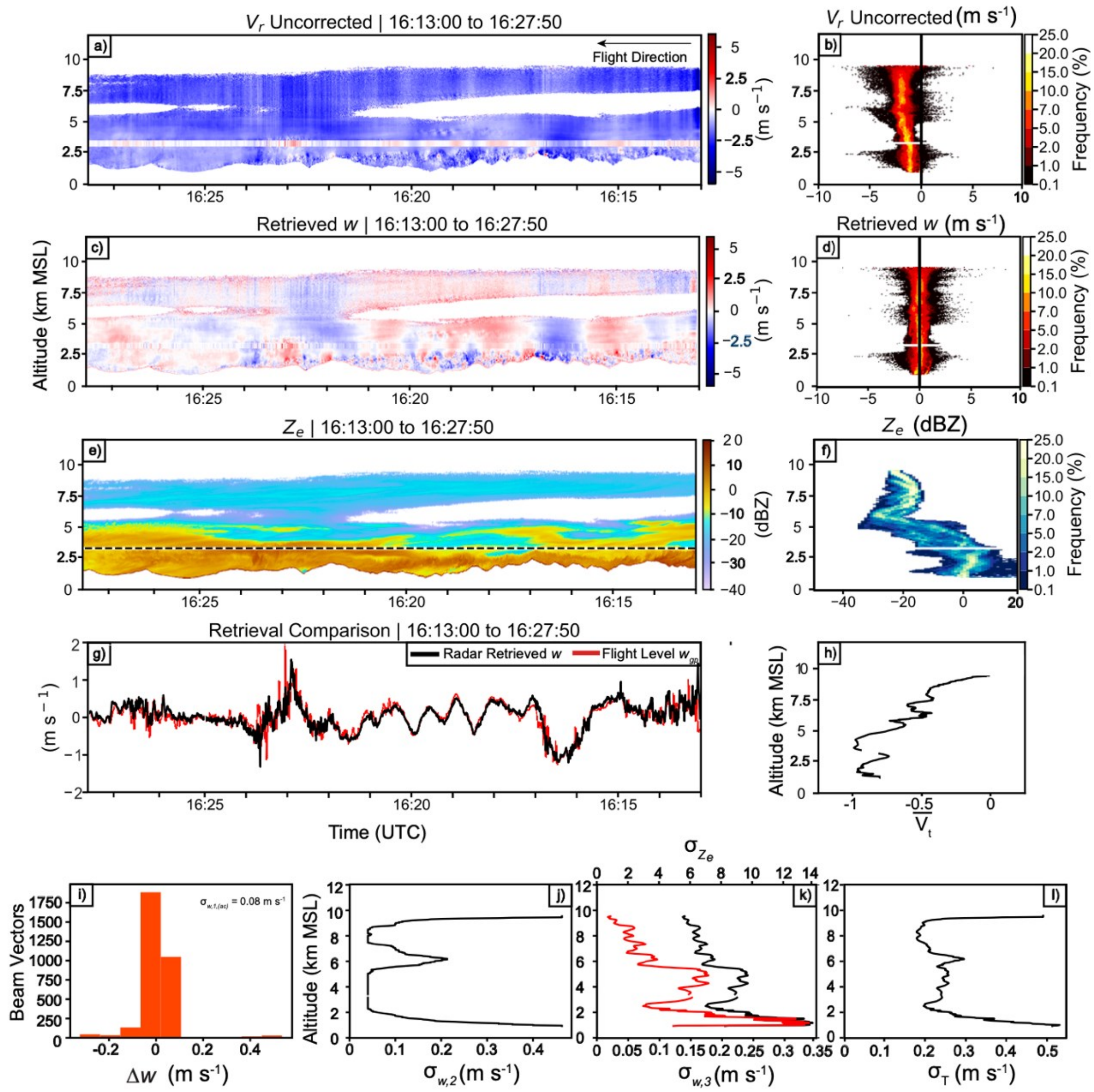

Fig. 8: Same as Fig. 7 except a southwest bound flight leg from IOP 21 from 7 March 2017 16:13:00 to 16:27:50 UTC. Southwest is on the left on panels (a), (c), (e), and (g).

Examining uncertainty associated with each of the three assumptions:

Assumption 1: $\sigma_{w,1}$ = ± 0.08 m s^{-1}, a consequence of differences between wind speed measured at flight level and the rawinsonde.

Assumption 2: $\sigma_{w,2}$= ± 0.04 m s^{-1} between 2.2-5 km and 7.4-8.5 km MSL where echo extent encompassed the entirety of the 76.1 km southwest flight leg. $\sigma_{w,2}$ = ± 0.46 m s^{-1} near cloud echo top (9.4 km) and at the surface (Figs. 8j). The split cloud layer present between 6-7 km had $\sigma_{w,2}$ = ± 0.09-0.22 m s^{-1}. Echo extent was limited in the split cloud layer to regions where the upper cloud layer was precipitating into the lower cloud layer.

Assumption 3: The Z_e CFAD (Fig. 8f) showed more variation at all m as a result of the layering structure. σ_{Z_e} was largest between surface and 2.5 km reaching 13.3 dBZ$_e$ with $\sigma_{w,3}$ = ±0.34 m s^{-1}. σ_{Z_e} = 3.4-8 dBZ$_e$ between 3.4-6.5 km with $\sigma_{w,3}$ = ± 0.18-0.24 m s^{-1} (Fig. 8k).

As a result, σ_T = ± 0.46-0.51 m s^{-1} within 200 m of the surface, decreasing to ± 0.19 m s^{-1} at 2.75 km (the minimum in the lower cloud layer), and then increasing toward cloud echo top of the lower cloud layer to ± 0.24 m s^{-1} (6.5 km) (Fig. 8l). σ_T = ± 0.29 to 0.49 m s^{-1} within 200 m of cloud echo top of the upper cloud layer and had a minimum σ_T = 0.21 m s^{-1} at 8.5 km. Comparison of w and w_{gp} show close correspondence near flight level (Fig. 8g), with MAE = 0.15 m s^{-1} along the flight leg. The MAE was less than σ_T (± 0.24 m s^{-1}) at flight level.

c) IOP 20 5 March 2017

IOP 20 sampled a complex cloud system over the Payette River Basin with high-amplitude gravity wave signatures in the V_r field between 4.5 km and 6.0 km and elevated convection apparent between 6 km and cloud echo top. Boundary layer turbulence was also present in the lowest 1 km above the terrain. The retrieved w showed that the gravity waves had maximum updrafts and downdrafts ranging from -7 m s^{-1} to 7 m s^{-1} (Fig. 9c,d). Vertical drafts were regularly spaced, and not related to the terrain as will be discussed in Part 2. Retrieved $\overline{V_t}$ was ~ -0.2 m s^{-1} near cloud echo top (8 km), decreasing with depth beneath cloud echo top to ~ -1 m s^{-1} at 2.5 km (Fig. 9h).

Examining uncertainty associated with each of the three assumptions:

Assumption 1: $\sigma_{w,1}$ = ± 0.23 m s^{-1}, a consequence of differences between wind speed measured at flight level and the rawinsonde (Fig 9i).

Assumption 2: $\sigma_{w,2}$ < ± 0.1 m s^{-1} between 1.9 and 8.2 km where echo extent encompassed the entirety of the 72.1 km flight leg (Fig. 9j). $\sigma_{w,2}$ = ± 0.46 m s^{-1} near the surface and cloud echo top.

Assumption 3: Z_e at all levels m had larger σ_{Z_e} than the previous two cases (Fig. 9k), increasing aloft where elevated convection was located (Fig. 9f). σ_{Z_e} exceeded 5 dBZ$_e$ throughout cloud depth except near cloud echo top. σ_{Z_e} increased near the surface to 15.2 dBZ$_e$ at 2.5 km. $\sigma_{w,3}$ increased with depth from ± 0.21 m s^{-1} near cloud echo top (8 km) to ± 0.34 m s^{-1} at ~2.5 km (Fig. 9j).

The result was that $\sigma_T = \pm$ 0.20-0.40 m s^{-1} between 1.8 and 7.8 km increasing to $\pm$ 0.49 m s^{-1} at cloud echo top and $\pm$ 0.58 m s^{-1} at the surface (Fig. 9l). *MAE* = 0.29 m s^{-1} along the flight leg and *MAE* was less than σ_T ($\pm$ 0.43 m s^{-1}) at the same level.

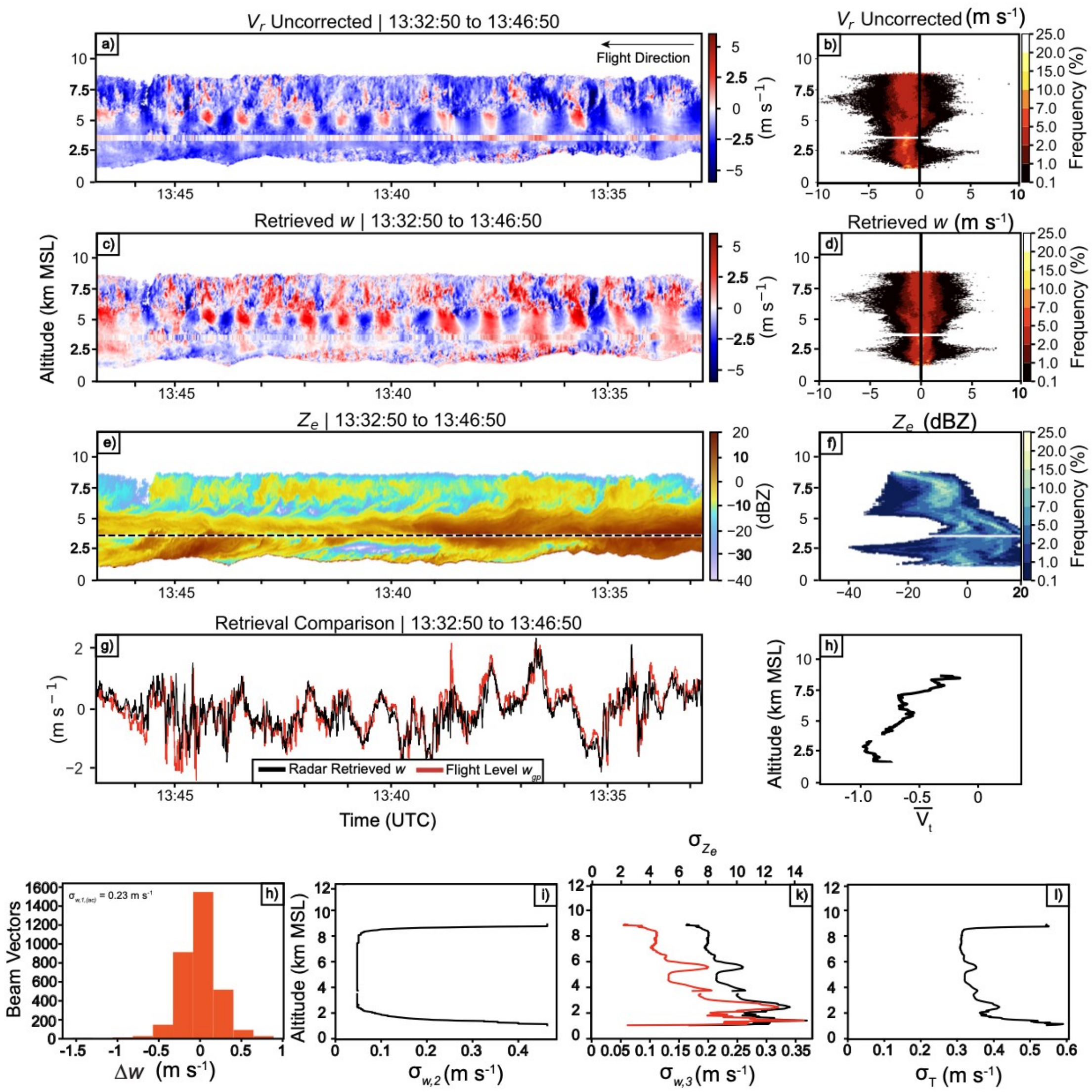

Fig. 9: Same as Fig. 7 but for a southwest flight leg from IOP 20 from 5 March 2017 13:32:50 to 13:46:50 UTC.

6. Examining scenarios with large uncertainty

The retrieval of w using the sounding correction for horizontal wind contribution presented above is best applied in deep stratiform cloud systems with uniform cloud coverage at all levels where large variations in particle V_t at a given level are not present. In the SNOWIE data, one situation was found to violate the assumption of constant $\bar{V}_t$ at a given a level, specifically a sloped melting level. Two additional situations were found to violate the assumption of uniform horizontal cloud extent: convective turrets and split layers. We illustrate these three problems below.

a) *Sloped Melting Level*

Figure 10 shows an example from IOP 23 where a sloped melting level was present decreasing in altitude from 2.8 km to 2 km as the aircraft traveled west to east over the Payette River Basin. Horizontal variation in the melting layer level resulted in an underestimation along the melting level of w on the western end of the flight leg and an overestimate of w along the eastern end of the flight leg, a result of over or under correction based on the subtraction of $\overline{V}_t$ along a non-homogenous feature at a constant grid level m.

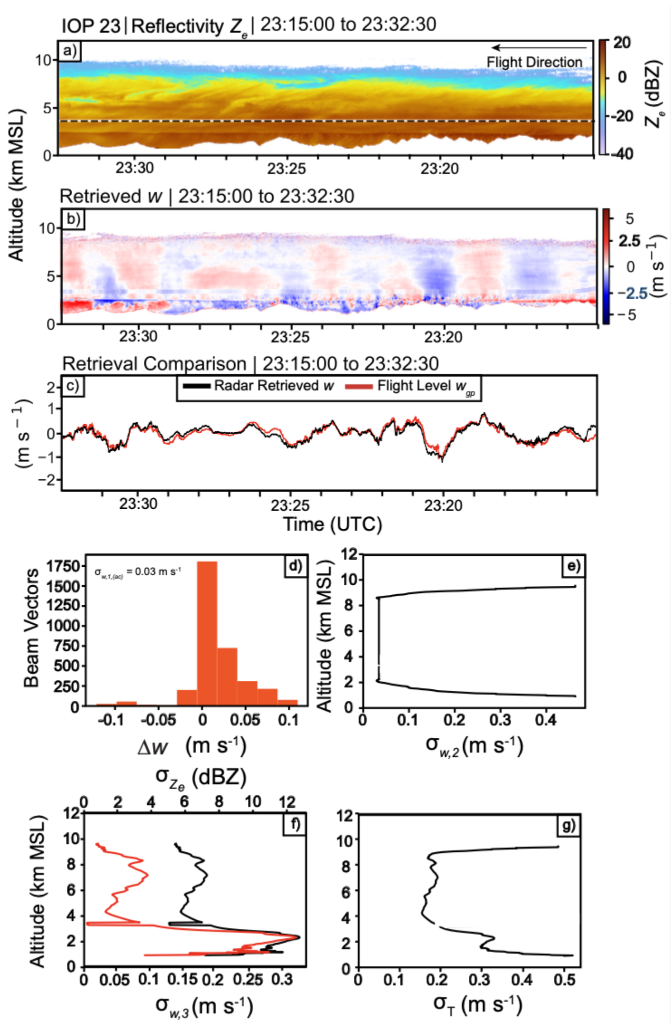

Fig. 10: Westbound flight leg during IOP 23 on 9 March 2017 from 23:15:00 to 23:32:30 UTC. (a) Z_e. The dashed black line is the aircraft flight level, (b) w, (c) comparison of w_{gp} (red) measured at flight level and radar retrieved w (black) from nearest range gates above and below the aircraft, (d) ΔW for nadir and zenith pointing beams, (e) $\sigma_{w,2,m}$, (f) $\sigma_{Z_{e,m}}$ (black) and $\sigma_{w,3,m}$ (red), (g) $\sigma_{T,m}$.

b) Convection

Figure 11a shows an example of elevated convection during IOP 12. The horizontal extent of cloud top echo was limited, consisting only of an elevated convective turret ~25 km wide. Examining uncertainty associated with assumptions 2 and 3:

Assumption 2: $\sigma_{w,2} = \pm$ 0.15-0.46 m s^{-1} between 5 and 6.6 km due to echo extent (Fig. 11d).

Assumption 3: The elevated convective turret had σ_{Z_e}= 11-14 dBZ$_e$ between 4-6 km with $\sigma_{w,3} = \pm$ 0.3 – 0.35 m s^{-1} (Fig. 11e).

As a result, σ_T was estimated to be ± 0.38 m s^{-1} near flight level. There were also large differences between retrieved w and w_{gp} measured at flight level with MAE = 0.62 m s^{-1} (Fig. 11c). These results show the impact of small echo extent along a given m on retrieval uncertainty.

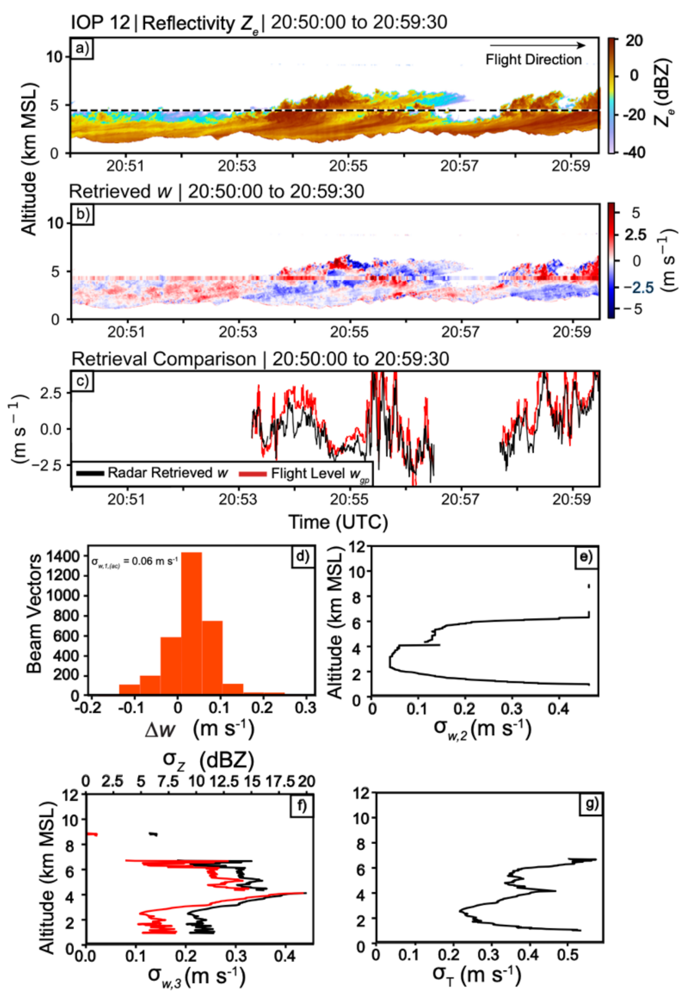

Fig. 11: Same as Fig. 10 except for an eastbound flight leg during IOP 12 on 7 February 2017 from 20:50:00 to 20:59:30 UTC.

c) Split Layers

IOP 3 sampled a split cloud layer along the western end of the flight leg and deep stratiform cloud along the eastern end (Fig. 12a, b). Along the western end of the flight leg, the lower cloud layer had Kelvin-Helmholtz waves near cloud echo top. The retrieved *w* along the western end of the flight leg had greater uncertainty due to inhomogeneities in Z_e along the leg. The value of σ_{Z_e} was < 5 dB above 6.1 km but beneath 6.1 km, the western half of the flight leg had low average Z_e (< 0 dBZ_e) and high Z_e on the eastern half of the flight leg (> 0 dBZ_e) associated with the deep precipitating orographic cloud. Throughout the split layer σ_{Z_e} > 10 dB reaching 25.8 dB at 4.3 km. As a result, $\sigma_{w,3} = \pm 0.5$ m s^{-1} at flight level (Fig. 12e). In this case there were also larger differences between retrieved *w* and w_{gp} measured at flight level with $MAE = 0.34$ m s^{-1} (Fig. 12c). The examples illustrated show that different events may have different sources of uncertainty when retrieving *w*.

7. Summary of *w* retrieval uncertainty on all flight legs

The retrieval method presented in Sec. 3 was applied to obtain *w* and $\overline{V_t}$ for the entire SNOWIE dataset. Figure 13 shows a summary of σ_T as a function of all retrieved *w* values during the 23 SNOWIE research flights. Figure 13b shows that 67% of retrieved *w* values had updrafts/downdrafts between ±0.71 m s^{-1} over the Payette River Basin and 95% of retrieved *w* values had *w* between ±1.42 m s^{-1}. Most updrafts were relatively weak associated with stratiform ascent/descent within fixed orographically-induced waves. The range of σ_T typically increased as the magnitude of updrafts/downdrafts increased. Median σ_T increased from 0.22 m s^{-1} to 0.39 m s^{-1} as *w* increased from 0 m s^{-1} to ±10 m s^{-1}. The 95th percentile of σ_T increased from 0.43 m s^{-1} to 0.62 m s^{-1} as *w* magnitude increased from 0 m s^{-1} to ±10 m s^{-1}. The 5th percentile increased slightly from 0.18 m s^{-1} to 0.23 m s^{-1} as *w* increased from 0 m s^{-1} to ±10 m s^{-1}. Stronger updrafts and downdrafts were typically associated with a wider range of uncertainties. For example, an updraft between 4.5 – 5 m s^{-1} had a median σ_T of ~0.4 m s^{-1}, while an updraft of 0 – 0.5 m s^{-1} had a median σ_T of ~0.2 m s^{-1}.

To further evaluate the performance of the *w* retrieval, each flight leg during SNOWIE was interrogated. For these legs, retrieved *w* above the aircraft and below the aircraft was averaged and compared to w_{gp}, resulting in 59,701 collocated *w* and w_{gp} measurements (Fig. 14). The absolute difference $|w - w_{gp}|$ was calculated for all samples and the distribution of these values is shown as in Fig. 14. The median $|w - w_{gp}|$ was 0.18 m s^{-1} and the mean was 0.27 m s^{-1}.

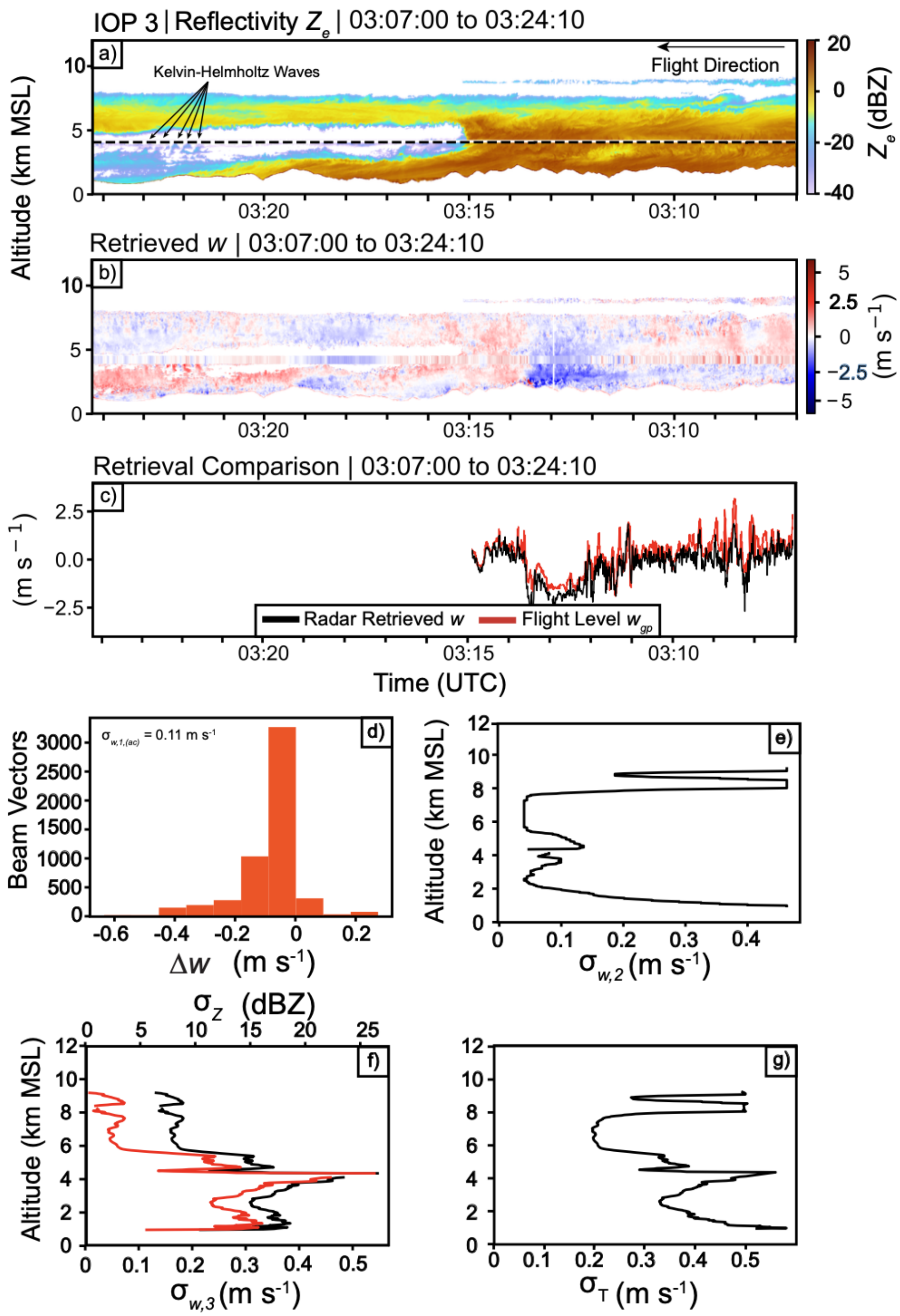

Fig. 12: Same as Fig. 10 except for a westbound flight leg during IOP 3 on 11 January 2017 from 03:07:00 to 03:24:00 UTC.

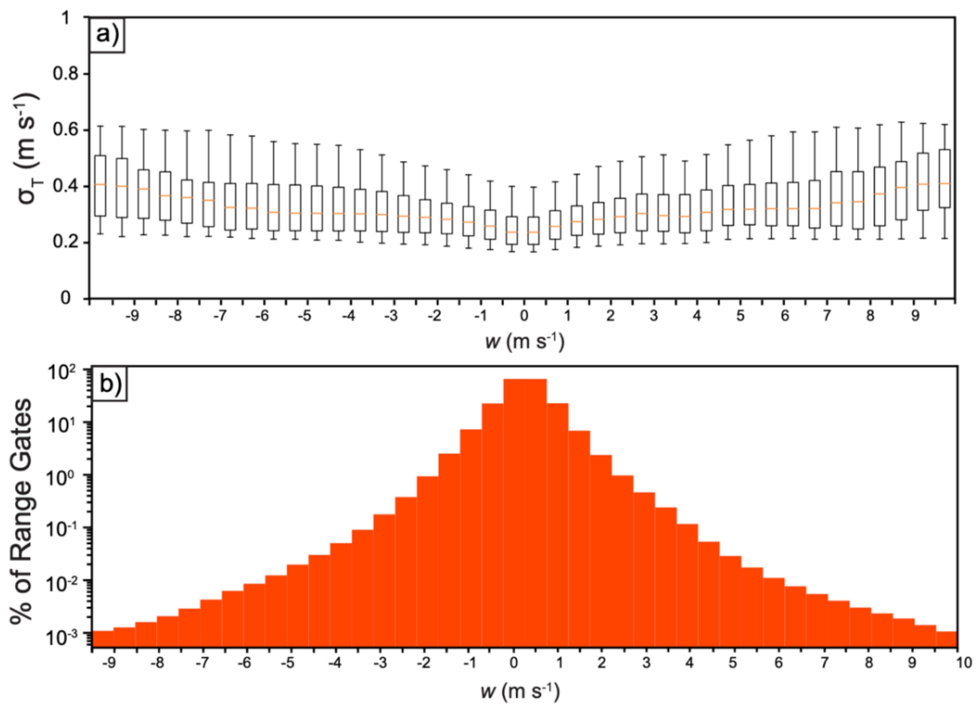

Fig. 13: a) Boxplots of σ_T for all w values during SNOWIE binned every 0.5 m s^{-1}. Orange lines denote median σ_T for a given w bin. The upper bound of the box represents the 75th percentile of σ_T while the lower bound of the box represents the 25th percentile of σ_T. The whiskers represent the 5th and 95th percentile of σ_T. b) the percentage of w values sampled during SNOWIE.

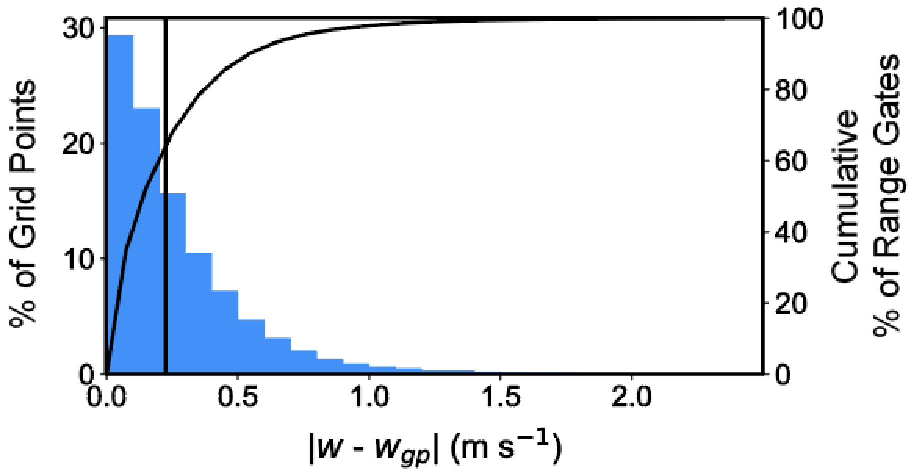

Fig. 14: $|w - w_{gp}|$ for all collocated UWKA w retrievals and w_{gp} data points as a percentage on the left axis. The black curve and right axis show the cumulative percentage. The vertical black line represents the median $|w - w_{gp}|$.

8. Conclusions and Discussion

This paper presented an analysis of uncertainties associated with assumptions made when retrieving vertical air motion (w) and mean profiles of reflectivity-weighted terminal velocity ($\overline{V_t}$) from airborne measurements of Doppler radar radial velocity (V_r) from the nadir and zenith WCR antennas. This retrieval methodology and its assumptions are directly applicable to any airborne vertically-pointing Doppler radars. Assumptions were tested in orographic clouds over the Payette River Basin of Idaho sampled during the Seeded and Natural Orographic Wintertime Clouds: the Idaho Experiment (SNOWIE).

The retrieval technique for extracting w and $\overline{V_t}$ from V_r involves correcting V_r for known pitch, roll, and yaw angle deviations due to aircraft motion using the magnitude of the horizontal wind components (u,v) at a given height measured independently by a rawinsonde. This allows for the retrieval of vertical radial velocity, W, effectively the hydrometeor vertical velocity, from which w and $\overline{V_t}$ can be retrieved. The accuracy of the retrieval of w and $\overline{V_t}$ was assessed and shown to be dependent on satisfying assumptions that (a) the flight legs occur over a short enough time and distance that the along and across track winds at a given altitude above/below the aircraft do not vary horizontally or change with time, (b) the legs are long enough for the magnitudes of the updrafts and downdrafts at any given altitude to sum to 0 m s^{-1}, and (c) that the reflectivity-weighted hydrometeor $\overline{V_t}$ does not vary substantially at a given altitude, such that $V_{t,m}$ at any point along the flight leg can be approximated by $\overline{V_{t,m}}$. A method to estimate the uncertainty in the retrieval of w as a function of altitude was presented based on an evaluation of these assumptions. Each of these assumptions were evaluated quantitatively for example case studies and for the entire project dataset.

Case studies from SNOWIE research flights show that this methodology can provide estimates of w that closely matched measurements at the aircraft level. Deep stratiform precipitation with a rather flat cloud top and little Z_e variation at a given height is associated with the least retrieval uncertainty. The greatest uncertainty occurred in regions with isolated convective turrets, and at altitudes where split cloud layers were evident. Greater uncertainty also occurred in the presence a sloped melting level. Assumption (b) loses validity, and w cannot be reliably retrieved, near cloud top, and, in the presence of complex terrain, near the surface.

In Part 2 (Zaremba et al. 2022), we apply this retrieval technique to examine representative fixed and transient updraft structures present over the Payette River Basin of Idaho during SNOWIE and their relationship to thermodynamic forcing.

APPENDIX

Appendix A: Retrieval of *W* using a rawinsonde correction

The goal is to retrieve the vertical hydrometeor motion, $W = w - V_t$, along a radar beam from measured radial velocity V_r by removing contributions to V_r by aircraft motion and the horizontal wind.

The correction involves application of the transformation matrix, T_{A2G}, from aircraft to ground relative coordinates (x east-west, y north-south, and z up-down). T_{A2G} is the inverse of Haimov and Rodi (2013) where:

$$T_{A2G} = \begin{pmatrix} t_{11} & t_{12} & t_{13} \\ t_{21} & t_{22} & t_{23} \\ t_{31} & t_{32} & t_{33} \end{pmatrix}$$

$$= \begin{pmatrix} \sin(h)\cos(p) & \cos(h)\cos(p) & \sin(p) \\ \cos(h)\cos(r) + \sin(h)\sin(p)\sin(r) & -\sin(h)\cos(r) + \cos(h)\sin(p)\sin(r) & -\cos(p)\sin(r) \\ -\cos(h)\sin(r) + \sin(h)\sin(p)\cos(r) & \sin(h)\sin(r) + \cos(h)\sin(p)\cos(r) & -\cos(p)\cos(r) \end{pmatrix}$$

and *p*, *h*, and *r*, are the pitch, heading, and roll of the aircraft measured by the navigation system.

Let $\vec{b}$ be the calibrated beam-pointing vector in aircraft coordinates, $\overrightarrow{b_g}$, the beam-pointing vector in ground relative coordinates (where $\overrightarrow{b_g} = \vec{b}\,T_{A2G}$), $\overrightarrow{V_{ac}}$, the aircraft velocity vector in ground coordinates, and $\overrightarrow{V_s}$, the mean scatterer velocity vector in ground-relative coordinates where $\overrightarrow{V_s} = \vec{V} + \overrightarrow{V_t}$, where $\vec{V}$ is the 3D wind vector, and $\overrightarrow{V_t}$ is the pulse-volume average terminal velocity vector. V_r is equivalent to:

$$V_r = \overrightarrow{b_g} \cdot \left(\overrightarrow{V_{ac}} + \overrightarrow{V_s}\right) = \left(\vec{b}\,T_{A2G}\right) \cdot \left(\vec{V} + \overrightarrow{V_t} + \overrightarrow{V_{ac}}\right) \qquad (1)$$

The vectors in the x, y, and z directions in equation 1 are:

$$\vec{b} = (b_x, b_y, b_z)$$

$$\vec{V} = (u, v, w)$$

$$\overrightarrow{V_t} = (0, 0, -V_t)$$

$$\overrightarrow{V_{ac}} = \left(V_{ax}, V_{ay}, V_{az}\right)$$

Multiplying the beam pointing vector by the transformation matrix results in:

$$\left(\vec{b}\ T_{A2G}\right) = b_x t_{11} + b_y t_{21} + b_z t_{31} + b_x t_{12} + b_y t_{22} + b_z t_{23} + b_x t_{31} + b_y t_{32} + b_z t_{33}$$

The dot product of the beam transformation vector and the wind vector ($\vec{V}$) is:

$$\left(\vec{b}\ T_{A2G}\right) \cdot \left(\vec{V}\right) = \left(\vec{b}\ T_{A2G}\right) \cdot (u, v, w)$$

$$= b_x(t_{11}u + t_{12}v + t_{13}w) + b_y(t_{21}u + t_{22}v + t_{23}w) + b_z(t_{31}u + t_{32}v + t_{33}w)$$

This can be simplified as:

$$\left(\vec{b}\ T_{A2G}\right) \cdot (u, v, w) = b_{t1}u + b_{t2}v + b_{t3}w$$

where:

$$b_{t1} = b_x t_{11} + b_y t_{21} + b_z t_{31}$$

$$b_{t2} = b_x t_{12} + b_y t_{22} + b_z t_{32}$$

$$b_{t3} = b_x t_{13} + b_y t_{23} + b_z t_{33}$$

The dot product of the beam transformation vector and terminal velocity vector ($\overrightarrow{V_t}$) is:

$$\left(\vec{b}\ T_{A2G}\right) \cdot \left(\overrightarrow{V_t}\right) = -b_{t3}V_t$$

The dot product of the beam transformation vector and the aircraft motion vector ($\overrightarrow{V_{ac}}$) is:

$$\left(\vec{b}\ T_{A2G}\right) \cdot \left(\overrightarrow{V_{ac}}\right) = b_{t1}V_{ax} + b_{t2}V_{ay} + b_{t3}V_{az}$$

so that (1) becomes:

$$V_r = b_{t1}u + b_{t2}v + b_{t3}w - b_{t3}V_t + b_{t1}V_{ax} + b_{t2}V_{ay} + b_{t3}V_{az} \qquad (2)$$

Solving for w - V_t or W (vertical radial velocity) at each range gate:

$$W = w - V_t = \frac{V_r - (b_{t1}u + b_{t2}v + b_{t1}V_{ax} + b_{t2}V_{ay} + b_{t3}V_{az})}{b_{t3}}$$

The University of Wyoming King Air facility provides Level 1 and Level 2 data that is corrected for aircraft motion but not the horizontal wind contribution. The radial velocity provided by the facility, V_r', is:

$$V_r' = V_r - b_{t1}V_{ax} + b_{t2}V_{ay} + b_{t3}V_{az} = b_{t1}u + b_{t2}v + b_{t3}w - b_{t3}V_t \qquad (3)$$

For the provided data, corrected for aircraft motion, the retrieval of W for a single range gate becomes:

$$W = \frac{V_r' - (b_{t1}u + b_{t2}v)}{b_{t3}} \qquad (4)$$

Appendix B: List of variables and their descriptions

$\vec{b}$	calibrated beam pointing vector in aircraft coordinates
b_x	beam vector in x direction
b_y	beam vector in y direction
b_z	beam vector in z direction
$\overrightarrow{b_g}$	calibrated beam pointing vector in ground relative coordinates
h	heading
m	a given height (altitude) index
m_{ac}	aircraft altitude index
MAE	mean absolute error
n	beam index
p	pitch
r	roll
σ_T	total uncertainty
$\sigma_{w,1}$	uncertainty due to assumption 1
$\sigma_{w,2}$	uncertainty due to assumption 2
$\sigma_{w,3}$	uncertainty due to assumption 3
$\sigma_{\|w-w_{gp}\|}$	standard deviation of the absolute value of vertical air velocity minus vertical air velocity measured by the gust probe
$\sigma_{\Delta w}$	standard deviation of the difference in vertical radial velocity as a result of differences in rawinsonde measured winds and aircraft measured winds for all beams along a given flight leg
σ_{Z_e}	standard deviation of equivalent reflectivity factor
T_{A2G}	transformation matrix from aircraft to ground coordinates
u	zonal wind component
Δu	difference in the zonal wind component between the aircraft and sounding at the altitude of the aircraft for a given beam
v	meridional wind component
Δv	difference in the meridional wind component between the aircraft and sounding at the altitude of the aircraft for a given beam
$\vec{V}$	wind vector in aircraft relative coordinates
$\overrightarrow{V_{ac}}$	aircraft velocity vector in ground coordinates
V_{ax}	aircraft velocity in x direction
V_{ay}	aircraft velocity in y direction
V_{az}	aircraft velocity in z direction
$\overrightarrow{V_H}$	horizontal wind vector
V_r	measured Doppler radial velocity
V_r'	radial velocity corrected for aircraft motion but not horizontal wind contribution provided by the UWKA facility.
$\overline{V_r}$	mean measured Doppler radial velocity
$\overrightarrow{V_s}$	mean scatter velocity vector in ground relative coordinates
V_t	reflectivity weighted terminal velocity of hydrometeors
$V_{t,m}$	reflectivity weighted terminal velocity at a given height
$V_{t,m,n}$	reflectivity weighted terminal velocity at a given height along a given beam

$\overrightarrow{V_t}$	pulse-volume average terminal velocity vector
$\overline{V_{t,m}}$	mean reflectivity weighted terminal velocity at a given height
$\bar{V}_t$	mean reflectivity weighted terminal velocity of hydrometeors
w	vertical air velocity
w_{gp}	vertical air velocity measured by gust probe
$\bar{w}$	mean vertical air velocity
$w_{m,n}$	vertical air velocity at a given height along a given beam
$\overline{w_m}$	mean vertical air velocity at a given height
W	vertical radial velocity
Δw	difference in vertical air velocity as a result of differences in rawinsonde measured winds and aircraft measured winds
$W_{m,n}$	vertical component of radial velocity at a given height along a given beam
$\bar{W}$	mean vertical component of radial velocity
$\overline{W_m}$	mean vertical component of radial velocity at a given height
x	east-west direction
y	north-south direction
z	up-down direction
Z_e	equivalent reflectivity factor

Acknowledgments

We thank the crew from the University of Wyoming King Air (UWKA) as well as all students from the Universities of Colorado, Wyoming, and Illinois for their help operating and deploying instruments during the campaign. Funding for the UWKA and WCR during SNOWIE was provided through the National Science Foundation (NSF) award AGS-1441831. This research was supported under NSF Grants AGS-1547101, AGS-1546963, AGS-1546939, AGS-2016106, AGS-2015829, and AGS-2016077. We also thank Dr. Scott Collis and two anonymous reviewers for comments which helped substantially improve the quality of the paper.

Data Availability Statement

All data presented here are publicly available through the SNOWIE data archive website (https://data.eol.ucar.edu/master_lists/generated/snowie/) maintained by the Earth Observing Laboratory (EOL) at the National Center for Atmospheric Research (NCAR).

REFERENCES

Babb, D. M., J. Verlinde, and B. A. Albrecht, 1999: Retrieval of cloud microphysical parameters from 94-GHz radar Doppler power spectra. *J. Atmos. Oceanic Technol.*, 16, 489–503. https://doi.org/10.1175/1520-0426(1999)016<0489:ROCMPF>2.0.CO;2

Bergmaier, P. T., and B. Geerts, 2016: Airborne radar observations of lake-effect snow bands over the New York Finger Lakes. Mon. Wea. Rev., 144, 3895–3914, doi:10.1175/ MWR-D-16-0103.1.

Bergmaier, P. T., and B. Geerts, 2020: LLAP Band Structure and Intense Lake-Effect Snowfall Downwind of Lake Ontario: Insights from the OWLeS 7-9 January 2014 Event. *J. Appl. Meteor. Climatol.* 59 (10), 1691-1715, https://doi.org/10.1175/JAMC-D-19-0288.1

Bergmaier, P. T., B. Geerts, L. S. Campbell, and W. J. Steenburgh, 2017: The OWLeS IOP2b lake-effect snowstorm: Dynamics of the secondary circulation. *Mon. Wea. Rev.*, 145, 2437–2459, https://doi.org/10.1175/MWR-D-16-0462.1.

Chu, X., B. Geerts, L. Xue, and B. Pokharel, 2017: A case study of cloud radar observations and large-eddy simulations of a shallow stratiform orographic cloud, and the impact of glaciogenic seeding. J. Appl. Meteor. Climatol., 56, 1285–1304, https://doi.org/10.1175 /JAMC-D-16-0364.1

Damiani, R., and S. Haimov, 2006: A high resolution dual-Doppler technique for fixed multiantenna airborne radar. *IEEE Trans. Geosci. Remote Sens.*, **44**, 3475–3489. doi: 10.1109/TGRS.2006.881745

Delanoë, J., A. Protat, D. Bouniol, A. Heymsfield, A. Bansemer, and P. Brown, 2007: The characterization of ice cloud properties from Doppler radar measurements. *J. Appl. Meteor. Climatol.*, 46, 1682–1698. https://doi.org/10.1175/JAM2543.1

Deng, M., and G. G. Mace, 2006: Cirrus microphysical properties and air motion statistics using cloud radar Doppler moments. Part I: Algorithm description. *J. Appl. Meteor. Climatol.*, 45, 1690–1709. https://doi.org/10.1175/JAM2433.1

French J. R., S. Haimov, L. Oolman, V. Grubišić, S. Serafin, L. Strauss, 2015. Wave-induced boundary-layer separation in the lee of the Medicine Bow Mountains. Part I: Observations. *J. Atmos. Sci*, 72 (12), 4845-4863. https://doi.org/10.1175/JAS-D-14-0376.1

Geerts, B., and Q. Miao, 2009: Vertically pointing airborne Doppler radar observations of Kelvin–Helmholtz billows. *Mon. Wea. Rev.*, **138**, 982–986, doi:10.1175/2009MWR3212.1

Geerts, B., and Q.Miao, 2005: The use of millimeter Doppler radar echoes to estimate vertical air velocities in the fair-weather convective boundary layer. *J. Atmos. Oceanic Technol.*, 22**,** 225–246. https://doi.org/10.1175/JTECH1699.1

Geerts, B., Q. Miao, and Y. Yang, 2011: Boundary layer turbulence and orographic precipitation growth in cold clouds: Evidence from profiling airborne radar data. *J. Atmos. Sci.*, **68**, 2344–2365, doi:10.1175/JAS-D-10-05009.1.

Grasmick, C., and Geerts, B. 2020: Detailed Dual-Doppler Structure of Kelvin–Helmholtz Waves from an Airborne Profiling Radar over Complex Terrain. Part I: Dynamic Structure. *J. Atmos. Sci.*, 77 (5): 1761–1782. https://doi.org/10.1175/JAS-D-19-0108.1.

Grasmick, C., B. Geerts, J. R. French, S. Haimov, and R. M. Rauber, 2022: Estimating Microphysics Properties in Ice-dominated Clouds from Airborne Ka-W band Dual wavelength Ratio Reflectivity Factor in Close Proximity to in situ Probes. *Submitted to J. Atmos. Oceanic. Technol.*

Hagen, M., J. Delanoe, S. Ellis, F. Ewald, J. French, S. Haimov, G. Heymsfield, A. Pazmany, 2021: Airborne radar. In: Foken T (ed.), Handbook of Atmospheric Measurements. Springer Nature, Switzerland, 1099-1132. https://doi.org/10.1007/978-3-030-52171-4_39

Haimov, S., and A. Rodi, 2013: Fixed-antenna pointing-angle calibration of airborne Doppler cloud radar. *J. Atmos. Oceanic Technol.*, 30, 2320–2335, https://doi.org/10.1175/JTECH-D-12-00262.1.

Heimes, K., T. J. Zaremba, R. M. Rauber, S. A. Tessendorf, L. Xue, K. Ikeda, B. Geerts, J. French, K. Friedrich, R. M. Rasmussen, M. Kunkel, and D. Blestrud, 2022: Vertical Motions in Orographic Cloud Systems over the Payette River Basin Part 3: An evaluation of the impact of transient vertical motions on targeting during orographic cloud seeding operations. *Submitted to the J. Climate Appl. Meteor.*

Heymsfield, A. J., and J. Iaquinta, 2000: Cirrus crystal terminal velocities. *J. Atmos. Sci.*, 57, 916–938. https://doi.org/10.1175/1520-0469(2000)057<0916:CCTV>2.0.CO;2

Heymsfield, G. M., 1989: Accuracy of vertical air motions from nadir-viewing Doppler airborne radars. *J. Atmos. Oceanic Technol.*, 6, 1079–1082, https://doi.org/10.1175/1520-0426(1989) 006,1079:AOVAMF.2.0.CO;2.

Kollias, P., Albrecht B. A., and Marks F. Jr., 2002: Why Mie? *Bull. Amer. Meteor. Soc.*, **83 ,** 1471–1483. https://doi.org/10.1175/2010JTECHA1343.1

Liebe, H. J., T. Manabe, and G. A. Hufford, 1989: Millimeter-wave attenuation and delay rates due to fog/cloud conditions. *IEEE Transactions on Antennas and Propagation,* **37**, 1617-1612, doi:10.1109/8.45106.

Lenschow, 1972: The measurement of air velocity and temperature using the NCAR Buffalo Aircraft Measuring system. NCAR Tech. Note NCAR-TN EDD-75, 39 pp. http://dx.doi.org/10.5065/D6C8277W

Leon, D., G. Vali & , and M. Lothon, 2006: Dual-Doppler analysis in a single plane from an airborne platform. Part I: Technique. *J. Atmos. Oceanic Technol.*, **23**, 3–21. https://doi.org/10.1175/JTECH1820.1

Majewski, A., and J. French, 2020: Supercooled drizzle development in response to semi-coherent vertical velocity fluctuations within an orographic layer cloud. *Atmos. Chem. Phys.*, **20**, 5035–5054, https://doi.org/10.5194/acp-20-5035-2020.

Miao, Q., B. Geerts, and M. A. LeMone, 2006: Vertical velocity and buoyancy characteristics of coherent echo plumes in the convective boundary layer, detected by a profiling airborne radar. *J. Appl. Meteor. Climatol.*, **45 ,** 838–855. https://doi.org/10.1175/JAM2375.1

Mitchell, D. L., 1996: Use of mass-and area-dimensional power laws for determining precipitation particle terminal velocities. *J. Atmos. Sci.*, 53, 1710–1723. https://doi.org/10.1175/1520-0469(1996)053<1710:UOMAAD>2.0.CO;2

Orr, B. W., and R. A. Kropfli, 1999: A method for estimating particle fall velocities from vertically pointing Doppler radar. *J. Atmos. Oceanic Technol.*, 16, 29–37. https://doi.org/10.1175/1520-0426(1999)016<0029:AMFEPF>2.0.CO;2

Pazmany, A., R.McIntosh, R.Kelly, and G.Vali, 1994: An airborne 95 GHz dual-polarized radar for cloud studies. *IEEE Trans. Geosci. Remote Sens.*, 32**,** 731–739. doi: 10.1109/36.298002.

Pokharel, B., B. Geerts, X. Jing, K. Friedrich, K. Ikeda, and R. Rasmussen, 2017: A multi-sensor study of the impact of ground-based glaciogenic seeding on clouds and precipitation over mountains in Wyoming. Part II: Seeding impact analysis. Atmos. Res., 183, 42–57, https://doi.org/10.1016/j.atmosres.2016.08.018.

Protat, A., and C. Williams, 2011: The accuracy of radar estimates of ice terminal fall speed from vertically pointing Doppler radar measurements. *J. Clim. Appl. Meteor.*, 30, 2120-2137. https://doi.org/10.1175/JAMC-D-10-05031.1

Protat, A., S. Rauniyar, J. Delano, E. Fontaine, and A. Schwarzenboeck, (2019): W-band (95 GHz) radar attenuation in tropical stratiform ice anvils. *J. Atmos. Oceanic Technol*., 36(8),

Protat, A., Y. Lemaitre, and D. Bouniol, 2003: Terminal fall velocity and the FASTEX cyclones. *Quart. J. Roy. Meteor. Soc*., **129**, 1513–1535. doi: 10.1256/qj.02.68

Rosenow, A. R., D. M. Plummer, R. M. Rauber, G. M. McFarquhar, B. F. Jewett, and D.Leon, 2014: Vertical motions within generating cells and elevated convection in the comma head of winter cyclones. *J. Atmos. Sci.,* 71, 1538–1558, https://doi.org/10.1175/JAS-D-13-0249.1.

Tessendorf, S. A., J. R. French, K. Friedrich, B. Geerts, R. M. Rauber, R. M. Rasmussen, L. Xue, K. Ikeda, D. R. Blestrud, M. L. Kunkel, S. Parkinson, J. R. Snider, J. Aikens, S. Faber, A. Majewski, C. Grasmick, P. T Bergmaier, A. Janizeski, A. Springer, C. Weeks, D. J. Serke and R. Brunintjes, 2019: Transformational approach to winter orographic weather modification research: The SNOWIE Project. *Bull. Amer. Meteor. Soc*., 100(1), 71-92, https://doi.org/10.1175/ BAMS-D-17-0152.1

Vali, G., S. Haimov, 2001: Observed extinction by clouds at 95 GHz. TGRS, 39, 190-193, doi:10.1109/36.898682

Wang, Z., J French, G. Vali; P. Wechsler, S. Haimov, A. Rodi, M. Deng, D. Leon, J. Snider, L. Peng, A. L. Pazmany, 2012: Single aircraft integration of remote sensing and in situ sampling for the study of cloud microphysics and dynamics. *Bull. Amer. Meteor. Soc*., 93, 653–668. https://doi.org/10.1175/BAMS-D-11-00044.1

Wendisch, M. and J. -L. Brenquier, 2013: *Airborne Measurements for Environmental Research: Methods and Instruments*, Wiley-VCH Verlag GmbH & Co. KGaA, Weinheim, Germany, 655 pp, doi: 10.1002/9783527653218.

Zaremba, T. J., K. Heimes, R. M. Rauber, B. Geerts, J. R. French, C. Grasmick, S. Tessendorf, L. Xue, K. Friedrich, R. M. Rasmussen, M. L. Kunkel, and D. R. Blestrud, 2022: Vertical Motions in Orographic Cloud Systems over the Payette River Basin. Part 2: Fixed and

Transient Updrafts and their Relationship to Forcing. *Submitted to J. Appl. Meteor. Climatol.*